AGU PUBLICATIONS

JGR

Journal of Geophysical Research: Solid Earth

RESEARCH ARTICLE
10.1002/2015JB011895

Key Points:
- Statistical method for the identification of induced seismicity
- Our method enables assessment of regional potential of induced events
- Central CA shows only 4 likely induced sequences between 1980 and 2014

Supporting Information:
- Text S1 and Figures S1–S11
- Data Set S1
- Data Set S2
- Data Set S3
- Data Set S4
- Data Set S5
- Data Set S6
- Data Set S7
- Data Set S8

Correspondence to:
T. H. W. Goebel,
tgoebel@gps.caltech.edu

Citation:
Goebel, T. H. W., E. Hauksson, F. Aminzadeh, and J.-P. Ampuero (2015), An objective method for the assessment of fluid injection-induced seismicity and application to tectonically active regions in central California, *J. Geophys. Res. Solid Earth*, *120*, doi:10.1002/2015JB011895.

Received 16 JAN 2015
Accepted 7 SEP 2015
Accepted article online 29 SEP 2015

An objective method for the assessment of fluid injection-induced seismicity and application to tectonically active regions in central California

T. H. W. Goebel[1], E. Hauksson[1], F. Aminzadeh[2], and J.-P. Ampuero[1]

[1]Seismological Laboratory, California Institute of Technology, Pasadena, California, USA, [2]Department of Petroleum Engineering, University of Southern California, Los Angeles, California, USA

Abstract Changes in seismicity rates, whether of tectonic or of induced origin, can readily be identified in regions where background rates are low but are difficult to detect in seismically active regions. We present a novel method to identify likely induced seismicity in tectonically active regions based on short-range spatiotemporal correlations between changes in fluid injection and seismicity rates. The method searches through the entire parameter space of injection rate thresholds and determines the statistical significance of correlated changes in injection and seismicity rates. Applying our method to Kern County, central California, we find that most earthquakes within the region are tectonic; however, fluid injection contributes to seismicity in four different cases. Three of these are connected to earthquake sequences with events above *M*4. Each of these sequences followed an abrupt increase in monthly injection rates of at least 15,000 m^3. The probability that the seismicity sequences and the abrupt changes in injection rates in Kern County coincide by chance is only 4%. The identified earthquake sequences display low Gutenberg-Richter *b* values of ~0.6–0.7 and at times systematic migration patterns characteristic for a diffusive process. Our results show that injection-induced pressure perturbations can influence seismic activity at distances of 10 km or more. Triggering of earthquakes at these large distances may be facilitated by complex local geology and faults in tectonically active regions. Our study provides the first comprehensive, statistically robust assessment of likely injection-induced seismicity within a large, tectonically active region.

1. Introduction

The dramatic increase in the amount of wastewater that is produced as by-product of reservoir stimulation and hydrocarbon extraction is a growing concern for earthquake hazard in the U.S. Much of this wastewater is reinjected into high permeable formations via wastewater disposal (WD) wells, at times leading to fault slip and noticeable seismic activity [e.g., *Ellsworth*, 2013; *Frohlich and Brunt*, 2013]. Most major oil fields in central California exhibited a rapid increase in fluid injection rates by more than a factor of 2 between 2001 and 2013 (Figure 1), but potential seismogenic consequences have not been studied up to now. At a regional scale the number of earthquakes above *M*2 in central California shows no apparent correlation to the change in injection rates (Figure 1). The purpose of this study is to investigate whether small-scale induced earthquake sequences exist, hidden within high-background seismicity rates ($\dot{\lambda}_0$). (Note that the term "induced" in our study implies an anthropogenic component involved in a seismicity sequence. A clear distinction between triggering and inducing earthquakes is not attempted here. A more extensive discussion on earthquake triggering and contributions from different types of forcing is provided in section 6.4.)

Devising a systematic method for the detection of induced seismicity is complicated by the incomplete understanding of when and how fluid injection operations induce earthquakes. Induced seismicity is commonly assumed to be a result of pore pressure increase [*Evans*, 1966; *Healy et al.*, 1968; *Raleigh et al.*, 1976; *Kim*, 2013], poroelastic loading [*Segall et al.*, 1994], elastic stress changes resulting from large volumes of injected and extracted fluids [*Segall*, 1989], or a combination of these effects. In addition, several studies suggest that well operational parameters significantly influence the potential of inducing earthquakes. These parameters include injection rates [*Frohlich*, 2012], wellhead pressures [*Keranen et al.*, 2013], total injection volumes per well and formation [*McGarr*, 2014], and net production rates [*Brodsky and Lajoie*, 2013]. Local crustal conditions

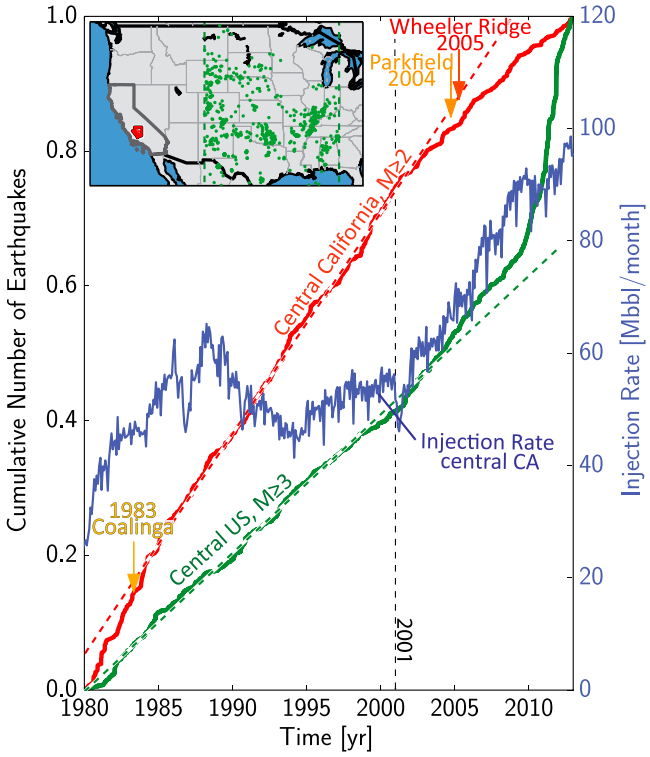

Figure 1. Comparison of seismic activity above *M*2 between central California (red curve) and the central U.S. (green curve). The dashed lines represent the average seismicity rates before 2001, and the blue curve shows the cumulative wastewater injection rate in millions of barrels (Mbbl instead of industry-standard MMbbl) in central California. Major historic earthquakes in greater Kern County after 1980 are highlighted by arrows and include the 1983 M_w6.4 Coalinga, the 2004 M_w6.0 Parkfield and the 2005 M_w4.6 Wheeler Ridge earthquakes. The cumulative earthquake numbers for central California exclude the areas of the Coalinga and Parkfield main shock and aftershocks. Many oilfields in central California show a strong increase in injection activity after ~2001, but an increase in seismic activity is conspicuously absent.

[*Frohlich and Brunt*, 2013; *van der Elst et al.*, 2013], the presence of critically stressed faults [*Deichmann and Giardini*, 2009], and static stress triggering [*Keranen et al.*, 2013; *Sumy et al.*, 2014] may further contribute to injection-related seismic hazard. More recently, reports of likely induced earthquakes due to high-volume fluid injection into vertically confined aquifers above basement lithological units are becoming more numerous [e.g., *Horton*, 2012; *Kim*, 2013; *Keranen et al.*, 2013].

Fluid injection and migration may occur over long periods and affect large areas thereby altering regional forcing rates and principal stress orientations [*Hainzl and Ogata*, 2005; *Martínez-Garzón et al.*, 2013; *Schoenball et al.*, 2014]. The likelihood of inducing earthquakes may be further enhanced if fluids can migrate beyond the intended geological formation [*Kim*, 2013; *Keranen et al.*, 2013].

Many previous studies focused on qualitative criteria for the identification of injection-induced seismic events in areas with low long-term background seismicity rates such as the central U.S. [e.g., *Davis and Frohlich*, 1993; *Frohlich*, 2012; *Frohlich and Brunt*, 2013; *Keranen et al.*, 2013; *Rubinstein et al.*, 2014]. These criteria include the spatial-temporal proximity between injection and seismic activity (including depth) and a noticeable change in seismicity rates. In California, only few studies attempted to link earthquake activity to fluid injection that was not associated with geothermal reservoirs [e.g., *Teng et al.*, 1973; *Kanamori and Hauksson*, 1992]. Extensive injection operations and high-seismicity rates within the last ~40 years make central California an excellent location to expand on and quantify previously suggested criteria for the detection of induced events.

This study is structured as follows: We first provide on overview of tectonic setting and utilized data sets. We then perform an exploratory examination of seismicity and injection data to identify injection patterns that can be parameterized for an automated analysis. We describe a new method for a uniform, quantitative assessment of potentially induced seismicity and apply it to Kern County, central CA. Lastly, we show the

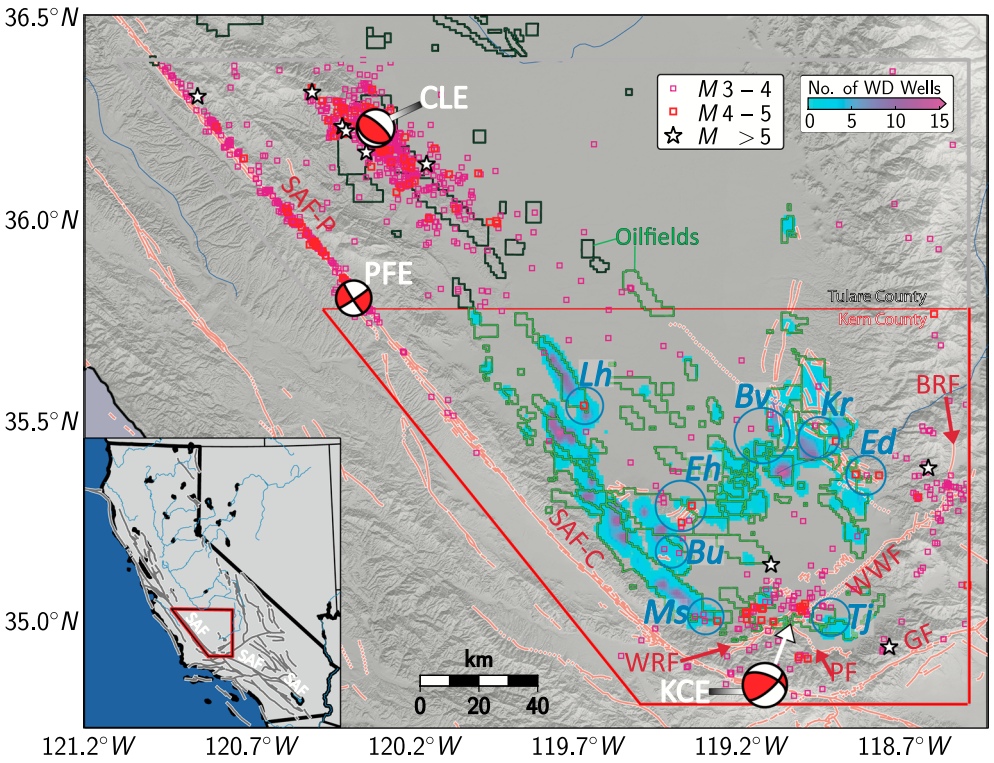

Figure 2. Seismicity above *M*3 (squares and stars), faults (red lines), and oilfields (green polygons) within San Joaquin Basin. Major faults include the Wheeler Ridge (WRF), Pleito (PF), Garlock (GF), White Wolf (WWF), and Breckenridge faults (BRF) as well as the Parkfield (SAF-P) and Carrizo (SAF-C) segment of the San Andreas Fault. The three largest earthquakes (red beach balls) are the 1952 M_w7.5 Kern County (KCE), the 2004 M_w6.0 Parkfield (PFE), and the 1983 M_w6.4 Coalinga event (CLE). The eight regions with $M > 3$ earthquakes close to active oil fields are highlighted by blue circles (*Ed*: Edison, *Kr*: Kern River, *Bv*: Bellevue, *Lh*: Lost Hills, *Eh*: Elk Hills, *Bu*: Buena Vista, *Ms*: Midway-Sunset, and *Tj*: Tejon). Magnitudes here and in the following figures are local magnitudes. The following analysis is limited to the area of Kern County within the red polygon. The larger region in this figure is displayed to capture some of the major historic seismic activity.

migration characteristics and frequency-magnitude distributions of likely induced seismicity sequences identified with our method.

2. Tectonic Setting and Data

Our study is focused on central California and includes the southern San Joaquin basin as well as seismically active faults to the west, east, and south of the basin. The tectonic deformation west of the basin is dominated by strike-slip faulting along the San Andreas Fault, while the east shows mainly normal faulting associated with the Breckenridge Fault. The tectonics south of the basin are characterized by a series of strike-slip and thrust faults, including the Wheeler Ridge, Pleito, and White Wolf faults [e.g., *Hardebeck*, 2006; *Yang and Hauksson*, 2013; *Unruh et al.*, 2014]. The latter produced the largest-magnitude earthquake within the study area, the 1952 M_w7.5 Kern County event (Figure 2). The recent, larger magnitude earthquakes to the north and south of the basin, none of which substantially changed the long-term background seismicity rates within the basin, are highlighted in Figure 1.

We analyzed the Advanced National Seismic System earthquake (ANSS) catalog between 1975 and 2014 which includes ~17,000 events from both the Southern and the Northern California Seismic Networks. The completeness magnitude, M_c, of the ANSS catalog is ~2.0 within the region, determined by inverting for the lower magnitude cutoff that minimizes the misfit between observed and modeled power law distributions [*Clauset et al.*, 2009; *Goebel et al.*, 2014a]. M_c varies in space and time, likely reaching higher values to the north and within the central part of the basin where the station density is low. However, the influence of M_c variations on the present study is small, because we compare relative changes in seismicity characteristics on small spatial-temporal scales as discussed below.

In addition to the ANSS catalog, we also use the waveform-relocated catalog by *Hauksson et al.* [2012] to obtain more accurate relative location uncertainties and focal depth estimates in areas with higher-station density south of the San Joaquin basin. Within the basin, large azimuthal gaps and event-station distances complicate depth estimates which is discussed in more detail in section 5 of Text S1 in the supporting information.

In the following, we correlate changes in seismicity and fluid injection rates ($\dot{V}_{inj}$) in wastewater disposal (WD) wells. The latter have been archived by the Division of Oil, Gas, and Geothermal Resources (DOGGR) of the California Department of Conservation since 1977 [*CA Department of Conservation*, 2012]. In addition to $\dot{V}_{inj}$, the DOGGR also archives wellhead pressures. The pressure data were not included in the present study for two reasons: (1) The wellhead pressure record is fragmentary and the statistical basis of the monthly documented values are not disclosed by the well operator and may vary for different wells. (2) The wellhead pressures may not be representative of reservoir pressures which are strongly influenced by structural heterogeneity [e.g., *Hsieh and Bredehoeft*, 1981].

The present analysis encompasses ~1400 WD wells in the study area south of the Kern county border (see Figure 2). Kern County is the largest oil-producing county in California, contributing more than 75% of California's total oil production and hosting more than 80% of the production and hydraulically fractured wells. Here each barrel of produced oil is accompanied by ~5–15 barrels of produced water highlighting that large volumes of wastewater have to be reinjected regularly [*CA Department of Conservation*, 2012]. In addition, water disposal can also include fluids from secondary reservoir stimulation like hydraulic fracturing. In the following, $\dot{V}_{inj}$ is given in thousands of barrel per month (kbbl/month), and 1 kbbl/month is equivalent to ≈160 m^3/month.

3. Initial Observations of $M > 3$ Earthquakes Close to Fluid Injection Wells

We performed a preliminary, exploratory examination of the injection and seismicity data resulting in an initial set of possibly induced earthquakes in Kern County. This preliminary data set was then used to guide the formulation of a more rigorous identification algorithm in section 4. For the initial and following analysis, we chose earthquake sequences containing events above a target magnitude of $M_T = 3$, which are events that can be felt by the nearby population.

During the exploratory data examination, we identified eight regions containing earthquakes above M_T with epicenters located within oil field boundaries or within a 10 km radius of active injection wells (Figure 2). For each earthquake above M_T, we determined whether a well within 10 km of the epicenters had fluid injection rates ($\dot{V}_{inj}$) above 100 kbbl/month at the time of the event. The choice for the initial injection rate threshold of 100 kbbl/month was guided by previous observations of likely induced seismicity [e.g., *Frohlich*, 2012]. We then visually examined the time series for possible correlations between seismicity rates ($\dot{\lambda}$) within a 10 km radius from the well and $\dot{V}_{inj}$. This examination revealed a variety of episodes of changes in injection rates within the spatiotemporal proximity of seismic activity, which generally showed two types of characteristics.

1. We observed earthquakes above M_T that were associated with local injection maxima (e.g., in 1991 and 2000 in Figure 3a). These maxima in injection rates were preceded by months to years of sustained increase in injection rates. In addition, one region showed a long-term positive correlations between $\dot{\lambda}$ and $\dot{V}_{inj}$ superimposed on the short-term correlation (Figure 3b).
2. We observed seismic activity close to injection sites with abrupt jumps in $\dot{V}_{inj}$ without long-term sustained increase (Figure 4). Such a site is for example located at the southern end of the Lost Hills oil field which in turn is located to the northwest of Kern County (*Lh* in Figure 2). The injection well *Lh* was active between 1986 and 1995 and displays a strong short-term correlation between a rapid increase in injection rates in February 1988 and a M_L4.2 earthquake sequence that occurred at a distance of less than ~0.5 to 1.5 km on 22 February 1988.

In the following, we use these preliminary observations to guide the formulation of a more rigorous identification algorithm. This algorithm searches through the entire parameter space of injection rate thresholds.

4. Objective Induced Seismicity Correlation Method

4.1. Main Concepts and Criteria of Correlation Method

We developed a set of rigorous statistical measures that quantify the significance of short-range spatiotemporal correlations between injection and seismicity rate changes. The method developed here is referred

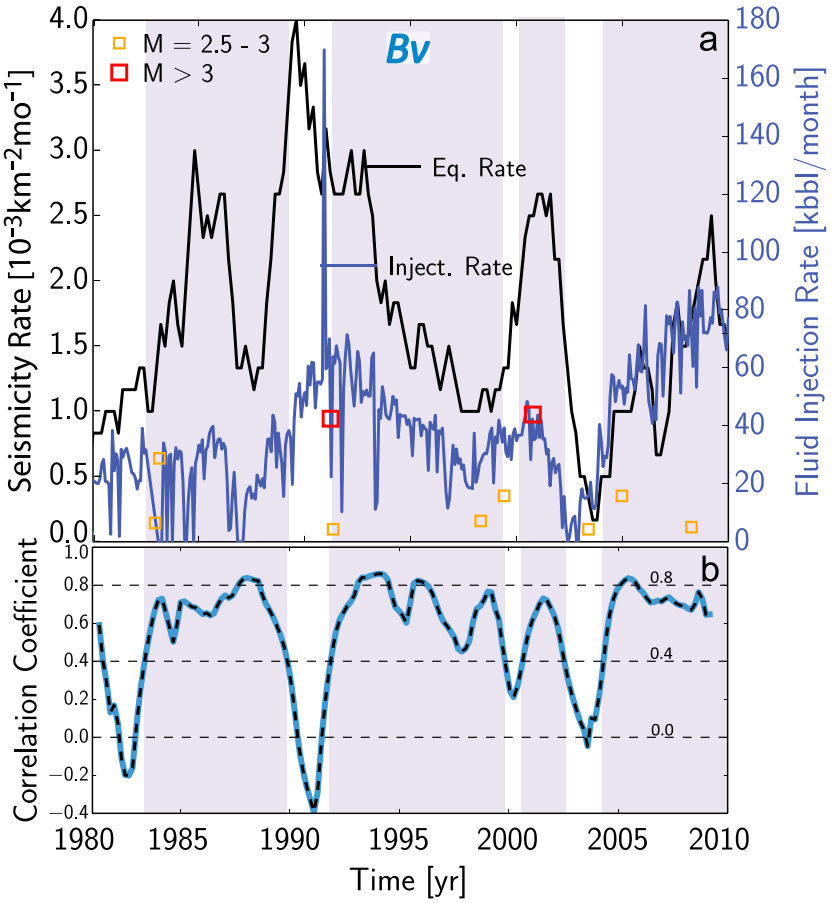

Figure 3. (a) Injection rates, $\dot{V}_{inj}$ (blue), and seismicity rates, $\dot{\lambda}$ (black), for events above *M*2 and within 10 km of the well as well as events above *M*2.5 (colored squares). The vertical positions of the squares correspond to relative differences in magnitudes. $\dot{\lambda}$ and $\dot{V}_{inj}$ display a noticeable long-term correlation. (b) Temporal variations in cross-correlation coefficients for $\dot{V}_{inj}$ and $\dot{\lambda}$ within a sliding time window of 2 years and a 10 km radius from injection site *Bv* in Figure 2. Higher-frequency variations in seismicity and injection rates were removed using a five-point median filter, prior to correlating the two time series.

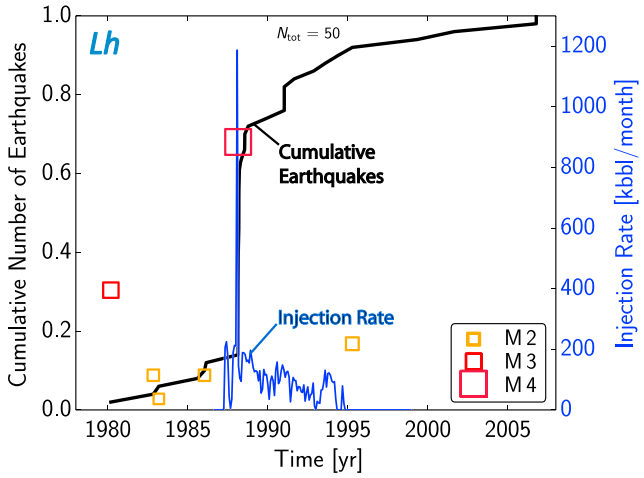

Figure 4. Injection rates (blue), cumulative earthquake number (black), and earthquake magnitudes (colored squares) within a 10 km radius of injection well *Lh*. (See also Figure 10c for short-term behavior close to injection).

Table 1. Identification Criteria for Likely Induced Seismicity Sequences[a]

	Description of Criteria	Parameter	Section
1	Episodes of changes in injection rates and seismic activity above M_T are associated in space and time.	r, Δt	4.3
2	The probability that the number of events above M_T part of the background seismicity is low. This probability is computed for events above M_T within r, and Δt based on the background rates within the region.	P_{poi}	4.4
3	The probability that episodes of changes in injection rates coincide with earthquakes above M_T by chance is low, given the local injection and seismic activity.	P_{ran}	4.5
4	The seismicity rate is significantly higher after, compared to before an episode of injection rate change. Seismicity rate changes are determined using the R statistic of *Felzer and Brodsky* [2005] and *van der Elst and Brodsky* [2010].	R	4.6

[a]A detailed description of each criteria and connected parameters can be found in the sections listed in the last column. A step-by-step summary of the algorithm is provided in section 4.7 and in a flow chart in the supporting information.

to as "Objective Induced Seismicity Correlation (OISC) Method." The main concepts of the method are summarized in the following table (Table 1):

4.2. Location and Onset of Injection Rate Changes

First, we specify a suite of targets for the OISC method including a wide range of injection rate thresholds and two different types of injection activity. The latter include a gradual and an abrupt increase in $\dot{V}_{inj}$. In the following, the specific types of injection activities are referred to as type *a* (gradual) and type *b* (abrupt) triggers, respectively (Figure 5). We use the term "trigger" to highlight the potential seismogenic consequences of specific types of injection operations, although not every trigger is associated with seismicity or is expected to result in seismicity given the many injection wells and modest seismic activity. The onset for each theoretical trigger was determined after smoothing the injection data with a five-point (5 months) median filter, to remove high-frequency fluctuations and isolated spikes. To avoid multiple considerations of the same trigger as a result of the median filtering, we required a separation of at least 5 1/2 months between each onset. The onset of a gradual, type *a* trigger is defined as the month when injection rates exceed a threshold value, $\dot{V}_{th}$, following a monotonic increase in $\dot{V}_{inj}$ over at least 3 months. The onset of an abrupt, type *b* trigger is defined as the month after a sudden increase in $\dot{V}_{inj}$ by a value above $\dot{V}_{th}$. For each disposal well in Kern county, we determined the onset of all types *a* and *b* triggers for a wide range of injection thresholds and test for short-term correlations with nearby seismicity as outlined in the following sections.

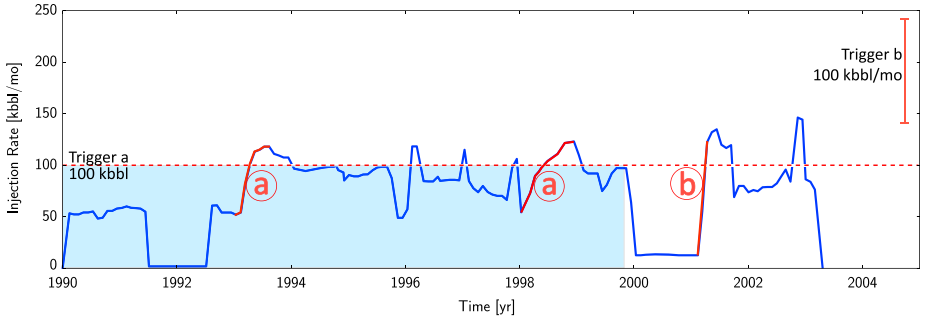

Figure 5. Example of injection rates at a WD well that can be categorized into two type *a* triggers and one type *b* trigger. Type *a* triggers are defined as a gradual increase in $\dot{V}_{inj}$, whereas type *b* triggers are defined as an abrupt in monthly injection rates (see text for details).

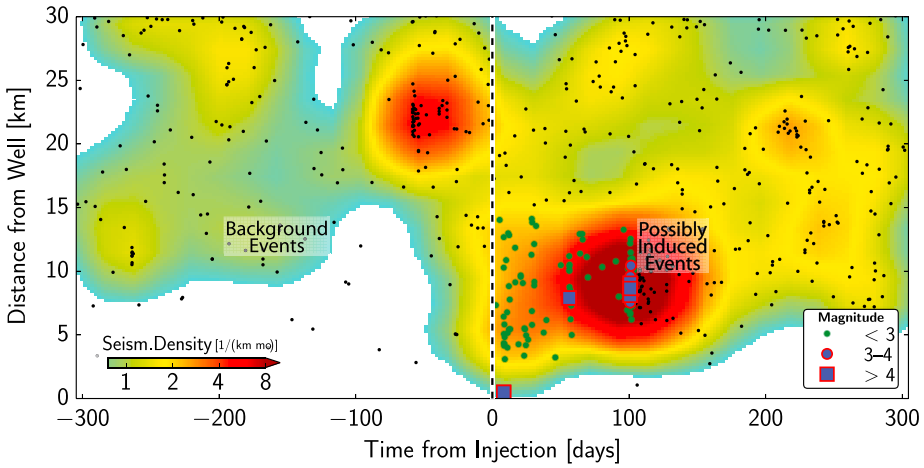

Figure 6. Seismicity density of stacked, candidate-induced earthquake sequences, 300 days before and after injection rate peaks of wells with the highest spatial-temporal correlations of the initial analysis scheme. The background seismic activity is highlighted by black markers, possibly induced events by green dots as well as red circles ($M > 3$) and rectangles ($M > 4$). The criteria for initial candidate event selection are described in section 3 . The M_L 4.2 event close to *Lh* (see Figure 4) is easily recognizable at the origin of injection.

4.3. Physical and Observational Constraints on Space-Time Windows

Induced seismic events occur predominantly within a limited space-time window from the injection operations. The extent of this window is governed by the underlying physical processes which include, for example, poroelastic stresses and pore pressure perturbations. Here we assume that the size of the space window is related to the time window by an underlying diffusive process via the following equation [e.g., *Shapiro et al.*, 1997]:

$$r = \sqrt{4\pi D \Delta t}, \tag{1}$$

where r is the distance from the wellhead, Δt is the maximum extent of the time window, and D is hydraulic diffusivity. Here we chose a value of D=2 m^2/s providing an upper limit for the injection-affected area based on published values which generally range between 0.2 and 1 m^2/s [e.g., *Shapiro et al.*, 1997; *Hainzl and Ogata*, 2005].

The maximum time window for declaring an association between a trigger and seismicity can be guided by background seismicity rates (see section 4.4) and empirically observed differences in seismicity density before and after trigger onset. To this aim, we stacked and centered the seismicity sequences from the exploratory data examination at the month of peak injection and computed seismicity density variations as a function of time and epicentral distance from injections (Figure 6). The seismicity density was determined using a Gaussian smoothing kernel with a width of 3 km/month. The highest densities occur in close temporal proximity of episodes of injection rate changes. Based on these seismicity density estimates, we selected an upper limit for the time window of interest of $\Delta t = 110$ days. Using this value and equation (1), we determined a maximum distance from injection of $r = 15.45$ km.

4.4. Background Rates, Poisson Probability, and Statistical Constraints on Space-Time Windows

The OISC method includes three statistical measures that reveal the strength of correlations between episodes of injection rate changes and earthquakes above M_T. These measures correspond to criteria 2–4 in Table 1. The first statistical measure reveals whether the number of events above M_T conforms to the number of events expected from a stationary Poissonian process with constant rate $\dot{\lambda}_0$ within a specific region. To compute $\dot{\lambda}_0$, we declustered the earthquake record following *Gardner and Knopoff* [1974], assuming that earthquake occurrences with aftershocks removed are independent in time. The probability, P_{poi}, of k earthquake occurrences within a given space-time-magnitude window is then given by

$$P_{poi}(k; \dot{\lambda}_0) = \frac{(\dot{\lambda}_0 S \Delta t)^k e^{-(\dot{\lambda}_0 S \Delta t)}}{k!}, \tag{2}$$

where k is the number of candidate events above M_T, S ($= \pi r^2$) and Δt are the space/time window of interest and $\dot{\lambda}_0$ is the rate of independent main shocks within S over the duration of the seismic record (here 37 years). Since the removal of aftershocks is not a unique process [see, e.g., *van Stiphout et al.*, 2012], we examined the influence of main shock-aftershock clustering on P_{poi}. The values of P_{poi} changed only marginally for clustered versus declustered catalogs as a result of comparably low seismicity rates above M_T within the study area. While aftershock clustering is of minor influence in our study, it may have to be considered in other regions.

According to equation (2), an identifiable departure from the background seismicity due to a seismicity rate increase requires that $\dot{\lambda}_0 S \Delta t \ll k$. Combining this with the relation between space and time window sizes given in equation (1), we obtain the following constraint: $\Delta t^2 \ll k/(\dot{\lambda}_0 4\pi D)$. We determine an upper limit on the time window size, Δt_{max}, for which this constraint is satisfied even when dealing with very few events (very small k):

$$\Delta t_{max}^2 \ll \frac{1}{\dot{\lambda}_0 4\pi D}. \tag{3}$$

Equation (3) results in $\Delta t_{max} = 230 - 540$ days for observed variations in background seismicity rate between 0.018 and 0.098 $\frac{1}{km^2 yr}$. This rationale further supports that the choice of $\Delta t = 110$ days in the previous section is suitable to establish significant results considering the observed variations in $\dot{\lambda}_0$ within the study region. For regions with lower background seismicity rates such as the central and eastern U.S. even higher values of Δt can yield significant results.

4.5. Probability of Random Spatial-Temporal Coincidence of Injection and Seismicity Rate Variations

The second statistical test evaluates the null hypothesis that the short-term episodes of injection rate change and seismicity above M_T are a result of random coincidence. This test is warranted because seismicity rate changes are frequent and may be a result of natural triggering processes. The probability, P_{ran}, that injection and seismic activity coincide by chance depends on the length of the time series (N), the total number of months with detected events above M_T (K) within Δt, the number of type a or type b triggers (n), and the number of candidate-induced sequences (x) can be determined from a hypergeometric distribution:

$$P_{ran}(X = x) = \frac{\binom{K}{x}\binom{N-K}{n-x}}{\binom{N}{n}}. \tag{4}$$

The hypergeometrical distribution expresses the probability of obtaining x successes by simultaneous drawing n outcomes from a population that contains N members and a total of K successes. Here success is defined as a month associated with at least one seismic event above M_T within the space-time window constrained by r and Δt. For low injection rate thresholds, both n, and consequently, P_{ran} are expected to be large. In other words, if many different months within a time series are selected as triggers, the probability of one of these months being associated with seismic activity by chance will be large (depending on the overall observed, seismic activity). To avoid erroneous association of triggers and nearby seismicity (i.e., to reduce false detection) a restrictive threshold was chosen a priori and applied to the whole data set. P_{ran} generally depends on the overall variability and duration of injection activities as well as the seismicity rates, $\dot{\lambda}$ within a region. Using a 95% confidence level, we can reject the null hypothesis that the observed correlations are a result of random coincidence if $P_{ran} < 0.05$. This test also shows that an a priori definition of trigger criteria prevents subjective associations of injection activities with seismicity based on limited time series (see, for example, Figures S1 and S2 in the supporting information).

4.6. Seismicity Rate Changes and Significance

The last statistical test identifies seismicity rate increases and evaluates whether a particular increase is significant given the overall rate variability within a particular region. To this end, we employed the R statistic by *Felzer and Brodsky* [2005] and *van der Elst and Brodsky* [2010] which measures the average, relative change of time interval lengths between a trigger and two seismic events, i.e., the last before and first after its onset:

$$R = \frac{t_2}{t_1 + t_2}, \tag{5}$$

where t_1 and t_2 are the time intervals between the trigger and the two earthquakes as shown in Figure 7. The determination of the R statistic for a region incorporates information about the changes in spatial

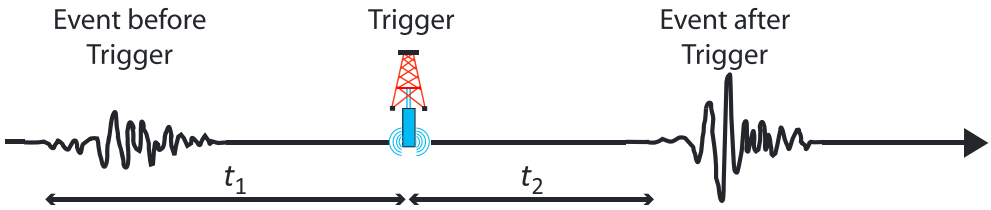

Figure 7. Sketch of the time interval ratio computed from the periods between the trigger onset and the last earthquake before and after.

seismicity clustering, which we implemented analogous to *Felzer and Brodsky* [2005] by discretizing the trigger surrounding area into 0.02° × 0.02° grid nodes. For each node, we determined the corresponding R value. We then computed the mean value over all nodes, $\overline{R}$ and confidence bounds from bootstrap resampling of all R values (see *van der Elst and Brodsky* [2010] for more details).

If no events are recorded before or after a trigger, only the minimum or maximum R value for a specific node is known. To diminish the statistical bias caused by catalog finiteness, we drew R values from random uniform distributions for nodes with missing events. If no event is recorded before the trigger, we determined a random R value with a lower bound which is a function of the catalog length before the trigger. If no event is recorded after the trigger a random R value was determined, bounded by the catalog duration after the trigger onset.

Values of $\overline{R}$ below 0.5 indicate that a trigger has on average advanced the timing of the following seismic events, corresponding to an increase in seismicity rates, $\dot{\lambda}$. The R ratio requires no specific time binning and relative changes within long time intervals and large areas can be detected which is important considering the expected temporal delay of earthquake triggering governed by diffusive processes. We tested the performance of the R statistic on synthetic catalogs from nonstationary Poisson processes with step increase in background rates and main shock-aftershock clustering according to an epidemic-type aftershock sequence model [e.g., *Felzer et al.*, 2002]. Our tests confirmed that the R statistic reliably detects rate changes even if these are only fractional changes of the original rates. For example, a step increase in rates by a factor of 1.5 results in $\overline{R} \approx 0.43$ which can reliably be identified relative to the background rate variations of an earthquake catalog with independent origin times (see Figure S3a in the supporting information). The synthetic tests also highlight that Poissonian and aftershock-dominated earthquake catalogs display high statistical variations in rates so that the significance of $\overline{R}$ values has to be established relative to the overall observed rate variations within a specific region. To this aim, we computed the significance level, p of $\overline{R}$, by drawing trigger onsets from a uniform random distribution over the catalog period (see supporting information section 3 for more details). The p value shows how significant a rate increase is given the overall rate changes in a region.

4.7. Summary of Steps and Thresholds Involved in the OISC Method

The OISC method, which can be applied to any region for which complete data sets of injection rates and seismicity are available, involves six main steps. These steps are summarized in the following (see also the flow chart in section S2 of Text S1 in the supporting information):

1. Define a trigger criterion, i.e., a specific type of injection rate change. For each type of trigger, search over parameter space of injection thresholds and determine onset times for each well and threshold.
2. Define a maximum time window, Δt, based on background seismicity rates and equation (3) and corresponding maximum distance, r (equation (1)), for the association of seismicity with injection activity. For each trigger in (1), identify if seismicity with events above M_T occurs within distance r from the well and time window Δt of the trigger onset.
3. For each trigger satisfying the criteria in step (2), compute Poissonian probability using the background seismicity rates and equation (2).
4. Compute the probability, P_{ran}, that injection and seismic activity coincide by chance using equation (4)
5. Compute the R statistic and evaluate the significance, p, of rate changes relative to trigger onsets.
6. Evaluate if earthquake sequences are likely induced based on statistical measures computed in step (3) to (5).

In the following, earthquake sequences are inferred to be induced if $P_{ran} < 0.05$, $P_{poi} < 0.05$, the upper confidence of $\overline{R}$ is below 0.5, and the statistical significance of $\overline{R}$ is below 0.15, i.e., $\overline{R}$ plots within the 15th

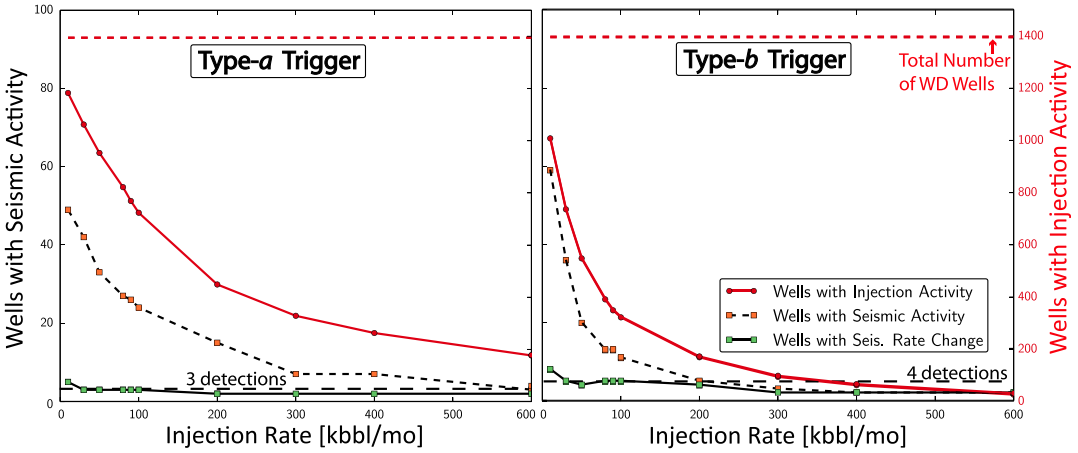

Figure 8. Number of wells that show (left) type *a* and (right) type *b* triggers. The total number of WD wells is ~1400 (red dashed line). The number of injection sites that also exhibit nearby seismic activity is highlighted by black, dashed curves. The number of injection sites associated with earthquake sequences according to the OISC method are highlighted by green curves. The dashed horizontal lines highlight the number of wells that were consistently correlated with earthquake sequences over the widest range of injection thresholds. Note that the red dashed lines and red curves are plotted at a different scale represented by the right *y* axis.

percentile of the overall observed rate changes. These threshold values were chosen conservatively and can be adapted depending on the local background seismicity rates. We varied trigger thresholds between 10 and 600 kbbl/month for both type *a* and type *b* triggers, and repeated steps 2 to 5 for all ~1,400 injection wells to assess if earthquake sequences are likely induced.

An exemplary application of the OISC method to a data set in central Valley, CA is described in the supporting information (section S3).

5. Results

5.1. Application of the OISC Method to Central California

From the total of ~1400 WD wells in Kern County, about 1200 wells inject wastewater at rates of at least 10 kbbl/month and also high injection rates of 600 kbbl/month are frequent, observed at ~200 wells (Figure 8). Seismicity occurs close to only a few of these wells. For example, we identified 50 wells with type *a* injection activity of at least 10 kbbl/month that also were spatially associated with seismicity within the above-defined spatial window. However, less than 20 out of 449 wells show nearby seismic activity for wells with type *a* injection rates above 200 kbbl/month. Applying the OISC method to greater Kern County, we find that 2–3 injection sites with type *a* and 2–4 with type *b* triggers are significantly correlated with seismicity (Figure 8). These wells are investigated in more detail in the following two sections.

The large-scale application of the OISC method to central California resulted in three general observations: (1) There is little seismic activity above M_T in spatial proximity to wastewater disposal sites. (2) The majority of both low- and high-rate injectors do not trigger seismicity sequences with events above M_L3. The relatively modest amount of potentially injection-induced seismicity is in agreement with the lack of large-scale seismicity rate increase after 2001 in Figure 1. (3) The likely earthquake-inducing injection sites, injected at rates of more than 100 kbbl/month (type *a* triggers) or 200 kbbl/month (type *b* triggers).

Several of the types *a* and *b* triggers are connected to the same earthquake sequence reducing the likely injection-affected areas to three, i.e., *Lh*, *Kr*, and *Tj* (Figure 9). In contrast to these three sites, injection at site *Bv* was only associated with a long-term correlation between seismicity rates of small events (M_L=2–3) shown in Figure 3. The two M_L3 earthquake sequences were not significantly correlated to changes in injection rates. The value of $P_{ran} \approx 0.16$ is high and based on the *R* statistic no significant rate increase could be detected. (Table 2). Thus, in the following injection at site *Bv* is treated separately .

The injection sites *Tj*, *Kr*, and *Lh* are located far apart toward the southern and eastern edge of San Joaquin Valley and within the valley. Three injection wells are located close to the M_L4.2 earthquake sequence within the Lost Hills oil field to the northwest of the study area. This sequence occurred in 1988 and is referred

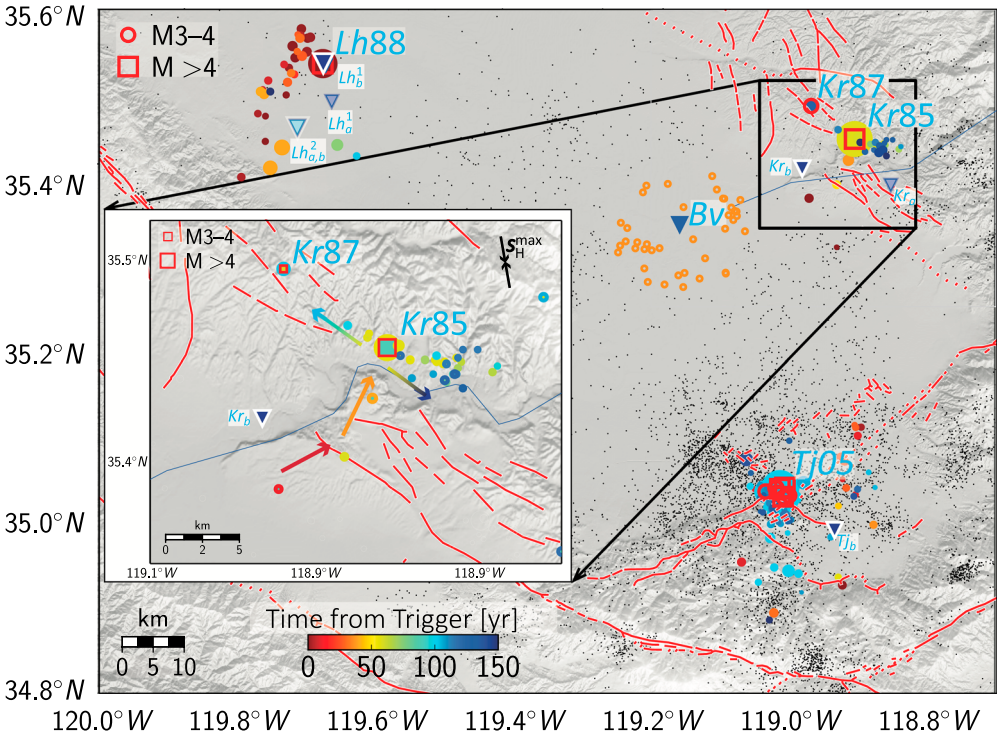

Figure 9. Locations of injection wells with type *a* (black bordered triangles) and *b* (white bordered triangle) triggers and nearby seismicity. Main shocks above *M*3 of earthquake sequences that were identified by the objective induced seismicity correlation method are labeled according to injection site and year of trigger occurrences. Seismicity (dots) is colored according to time after trigger onset and events above *M*3 are highlighted by red squares (see legend). The orange markers highlight the region of long-term correlation close to injection site *Bv*. Inset: Temporal migration of *Kr*85 and *Kr*88 seismicity sequences. Seismicity is colored according to time from trigger onsets at the closest injection sites. S_H^{max} orientation is taken from *Yang and Hauksson* [2013]. The injection rates for wells *Bv* and Lh_b^1 are shown in Figures 3 and 4.

to as *Lh*88. The closest trigger (Lh_b^1), which is approximately colocated with the main shock, was characterized by type *b* injection activity in 1988. The corresponding injection and seismicity rate changes were presented as part of the exploratory data examination in Figure 4. Although a contribution of several injection sites during the triggering of *Lh*88 may be possible, the close spatial-temporal proximity between the seismicity sequence *Lh*88 and the trigger Lh_b^1 suggest that the corresponding well was the predominant contributor to seismic activity.

Table 2. Results of Probabilistic Assessment for Well Locations and Nearby Seismicity Sequences[a]

Site	M_L^{max}/M_w^{max}	$\bar{R}$	p	P_{poi}	P_{ran}	$\dot{V}_{inj}$ (kbbl/month)	$\Delta\dot{V}_{inj}$ (kbbl/month)
Bv_a00	3.1/-	0.53 (0.468, 0.583)	0.553	<0.001	0.159	23	9
Bv_a91	3.1/-	0.46 (0.428, 0.527)	0.210	<0.001	0.159	153	102
Kr_b87	3.0/-	0.43 (0.389, 0.478)	0.120	0.013	0.001	1009	881
Kr_b85	4.6/-	0.40 (0.352, 0.452)	0.097	0.013	0.001	1055	725
Tj_b05	-/4.7	0.37 (0.300, 0.448)	0.024	0.004	0.026	352	216
Lh_b88	4.2/-	0.37 (0.317, 0.421)	0.009	0.010	0.032	1186	975

[a]Here we list only results for the closest well to a sequence. We also show results for $Bv91_a$ and $Bv00_a$, which did not meet the criteria for likely induced earthquakes. Site: Injection site, type of injection activity, and year of sequence; M_L^{max}/M_w^{max}: maximum magnitude within earthquake sequence; $\bar{R}$: *R* statistic, lower and upper confidence in parenthesis; *p*: significance of *R* statistic considering the overall observed rate changes within a region; P_{poi}: probability of earthquake occurrence as a function of $\dot{\lambda}_0$; P_{ran}: probability of random coincidence of trigger and earthquake sequence; $\dot{V}_{inj}$: injection rate at trigger onset; and $\Delta\dot{V}_{inj}$: change in injection rate compared to month before trigger onset.

We detected another likely induced earthquake sequence with a M_L4.6 event and two nearby wells, located to the northeast of the study area. The closest trigger, Kr_b^1, stems from a well with type *b* injection activity (Figure 9). In addition to being closer than trigger Kr_a^1, the nearby seismicity systematically migrated away from trigger Kr_b^1 in space and time (Figure 9, inset). This event migration pattern is discussed in more detail in the following section. We identified a fourth likely induced seismicity sequence close to injection site *Tj* south of San Joaquin Basin. In this case, only one injection well with type *b* injection activity was associated with the earthquake sequence in 2005 (*Tj*05).

Table 2 shows the results for the three wells with type *b* injection activity, as well as for the two type *a* triggers that preceded the $M > 3$ events close to *Bv* in 1991 and 2000 but where not significantly correlated with seismicity. Injection site *Kr* was connected to two $M \geq 3$ earthquake sequences: a M_L4.6 sequence in 1985 (*Kr*85) and a M_L3.0 sequence 1987 (*Kr*87). Because of the connected higher seismic activity the *p* value of the *R* statistic is also slightly higher than for the other sites but remained below the $p = 0.15$ significance threshold. In the following, we focus our analysis on the closest injection sites. These sites all showed type *b* injection activity.

5.2. Seismicity Migration and Timing Relative to Injection Activity

One possible difference between tectonic and induced events is the occurrence of smaller magnitude foreshocks which may migrate systematically away from the injection site [e.g., *Bachmann et al.*, 2012; *Skoumal et al.*, 2014]. Migration patterns that largely meet these criteria were observed close to injection site *Kr* where several smaller magnitude earthquakes preceded a M_L3 (*Kr*87) and a M_L4.6 (*Kr*85) main shocks (inset Figure 9). The migration path extends toward an unmapped fault which is parallel to known fault traces within the area and likely produced the 1985 M_L4.6 and 1987 M_L3.0 main shocks. Much of the seismicity concentrated along this fault which was likely activated by fluid injection, starting from the closest point of the fault trace to the injection site and migrating bilaterally along the fault. The systematic migration pattern becomes even more apparent when plotted as a function of time and distance from Kr_b (Figure 10a). Most of the seismicity connected to *Kr*85 and *Kr*87 fall within a space-time window that approximately agrees with a diffusive process governed by a hydraulic diffusivity of $D \approx 0.6–1.2$ m^2/s.

The seismicity sequence *Tj*05, on the other hand, showed no apparent systematic migration between injection site and the M_w4.7 main shock at the current level of catalog completeness (Figure 10b). Most of the seismicity falls within a space-time window limited by a diffusive process with $D = 1.2$ m^2/s, and about 140 days after the trigger, a M_L3 event occurred in close proximity to the $D = 1.2$ m^2/s diffusion curve. We observed some seismic activity prior to the main shock and seismicity rates increased slightly with the commencement of fluid injection in 2005, which may be injection related or part of the generally higher background seismicity within this region. More detailed analyses of the *Tj*05 events including underlying triggering processes and an analysis of the local geology go beyond the scope of this paper but will be addressed in a subsequent study.

Systematic spatial-temporal migration relative to the injection site are pronounced for seismicity sequence *Lh*88. This sequence began with the largest-magnitude event of M_L4.2 within ~1 km distance and migrated linearly in space and time away from the injection site (Figure 10c). The seismic activity was concentrated to the west of the well and showed a systematic migration approximately to south, possibly along a previously unmapped fault (Figure 9).

In addition to spatial-temporal migration, we investigated the relative timing of injection and seismic activity. The injection sites *Kr* and *Tj* exhibited a general time delay between fluid injection peaks and the following earthquake sequences that could be characteristic of a diffusive process. This time delay is also observed for injection site *Bv* which showed a long-term correlation between $\dot{V}_{inj}$ and $\dot{\lambda}$ for events with M_L=2–3. Assuming that the corresponding seismicity is triggered by fluid injection in site *Bv*, we can use the time lag between injection and seismicity rates to estimate the extent of the connected pore pressure perturbation as a function of hydraulic diffusivity. To this aim, we computed the correlation coefficient between $\dot{\lambda}$ and $\dot{V}_{inj}$ for increasing radii around the well, while simultaneously inverting for the time shift that maximizes the corresponding correlation coefficient (Figure 11). The coefficient is largest for a time lag of about 135 days and an affected area between 6 and 12 km which could be explained by a diffusive process with a diffusivity of $D = 0.3–0.8$ m^2/s (see red diamond in Figure 10a).

5.3. Frequency-Magnitude Distributions of Likely Injection-Induced Earthquakes

We investigated if fluid injection activity also influenced frequency-magnitude distributions and *b* values of nearby seismic events. We computed *b* values by using a maximum-likelihood estimate and magnitudes of

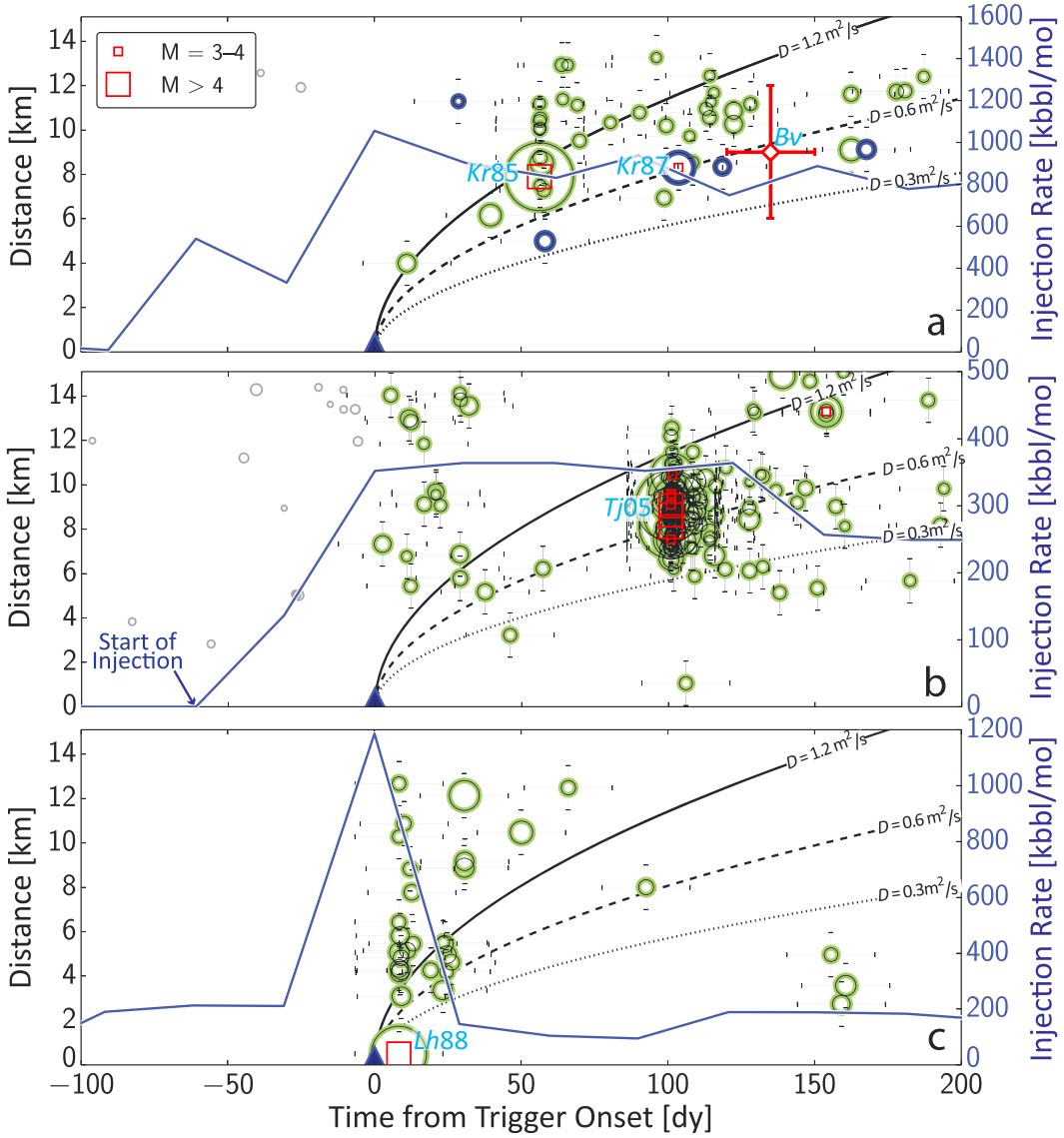

Figure 10. Spatial-temporal migration characteristics relative to the injection sites. Injection rates are shown by blue curves, and pore pressure diffusion curves by black dashed and solid lines. Seismicity prior to injection peaks is displayed by gray circles. (a) Seismicity and diffusion curves for *Kr*85 (green circles), *Kr*87 (dark blue circles), and *Bv* (red diamond), (b) *Tj*05, and (c) *Lh*88. Markers scale with magnitudes, and events above *M*3 and *M*4 are additionally highlighted by red squares. Vertical error bars show the average epicentral uncertainties in the ANSS catalog, and horizontal error bars correspond to uncertainties due to monthly reported injection rates which are mapped into the seismicity.

completeness by minimizing the fit between observed and modeled power law distributions [*Clauset et al.*, 2009; *Goebel et al.*, 2013, 2014b]. We started by estimating temporal variations in *b* values in the proximity of site *Tj*, using a sliding sample window of 150 events, thereby ensuring the same statistical significance of each data point. The *b* value estimates generally show relatively strong variations between 0.9 and 1.4 before the well became active in 2005 (Figure 12a). *b* values started to decrease after ~2003 with a short period of *b* value increase in 2004. Although *b* values start to decrease before the WD well under consideration became active, the cumulative wastewater disposal rates in the Tejon oilfield increased systematically within a similar time frame, starting in ~2001 [*CA Department of Conservation*, 2012]. The start of injection at well *Tj* coincided with a further decrease in *b* value down to its lowest level of 0.6 during peak injection rates. The *b* value recovered after $\dot{V}_{inj}$ was reduced by 30% toward the end of 2005. The postpeak injection *b* value remained ~0.2 beneath average, preinjection values.

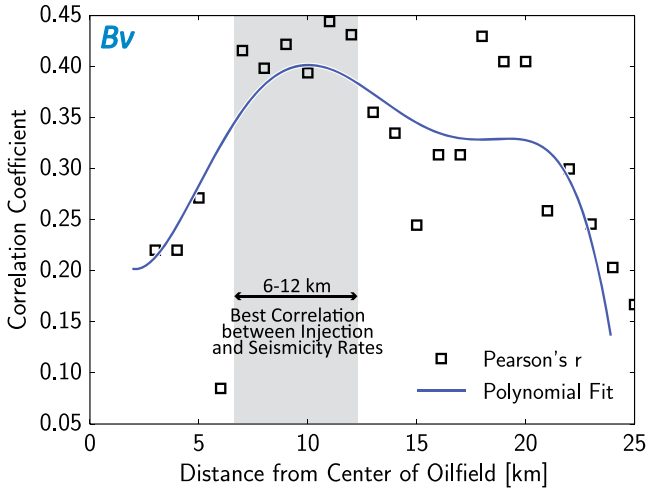

Figure 11. Correlation coefficient (Pearson's *r*) between $\dot{V}_{inj}$ and $\dot{\lambda}$ for seismicity at increasing distance from the injection site *Bv*. The correlations are estimated after shifting the two curves to maximize the correlation coefficient, and a polynomial fit (blue curve) was added to highlight the trend in correlation coefficients. The average time shift within the range of best correlation coefficients was $\Delta t \approx 135 \pm 15$ days.

We test the probability, P_b, that two different frequency-magnitude distributions originated from the same distribution using *Utsu* [1999]:

$$P_b = e^{\frac{-\Delta AIC}{2}-2}, \tag{6}$$

where ΔAIC is the difference in Akaike Information Criteria scores for two different power law fits [*Akaike*, 1974]. We determined a 9% probability that the prepeak and postpeak injection frequency-magnitude distributions originated from the same population. This probability is reduced to 0.1% when comparing the frequency-magnitude distributions during peak injection rates (~06–10/2005) with those after peak injection. In addition, the *b* value of ~0.6 during peak injection is significantly lower than other *b* value variations observed during 1980–2011 and falls below the minimum confidence limit of the average *b* value of unity (Figure 12c).

The results from temporal *b* value analyses of the other regions were not statistically significant because of comparably low seismicity rates. Nonetheless, a qualitative comparison of frequency-magnitude distributions indicates similarities between *Tj*, *Kr*, and *Lh*, i.e., relatively low *b* values of 0.6–0.7 (Figure 13) of seismic events that followed the trigger onset. The *b* value estimates in *Kr* and *Lh* are based on distributions with relatively few events resulting in high uncertainties.

6. Discussion

6.1. Statistical Significance of Detected, Likely Induced Sequences

Our results indicate that injection in four different wells likely contributed to seismic activity. These four wells are out of a total of ~1400 active disposal wells, of which only ~10% showed the abrupt changes in injection rates defined here as type *b* triggers. The likelihood that the described results occurred by chance is low for several reasons. First, the probability of earthquakes with specific magnitudes to occur within a specific space-time interval , as well as the occurrence of a specific type of injection activity (here type *a* or *b* triggers) within a limited space-time window is generally low, resulting in a low probability of random coincidence for the detected sequences (see Table 2). Second, the probability that the observed earthquake sequences coincide with injection triggers by chance given the total number of triggers within the study area is only ~4%. This probability was estimated by taking the three detected $M > 4$ events relative to the total of 12 main shocks with $M > 4$ within the study area and creating 1000 random catalogs assuming a random uniform distribution in space and Poissonian distribution in time.

Our study provides the first comprehensive, statistically robust assessment of likely injection-induced seismicity within a large area containing more than 1400 injection wells. We performed an initial exploratory data examination to identify injection patterns that could be formally parameterized for an objective,

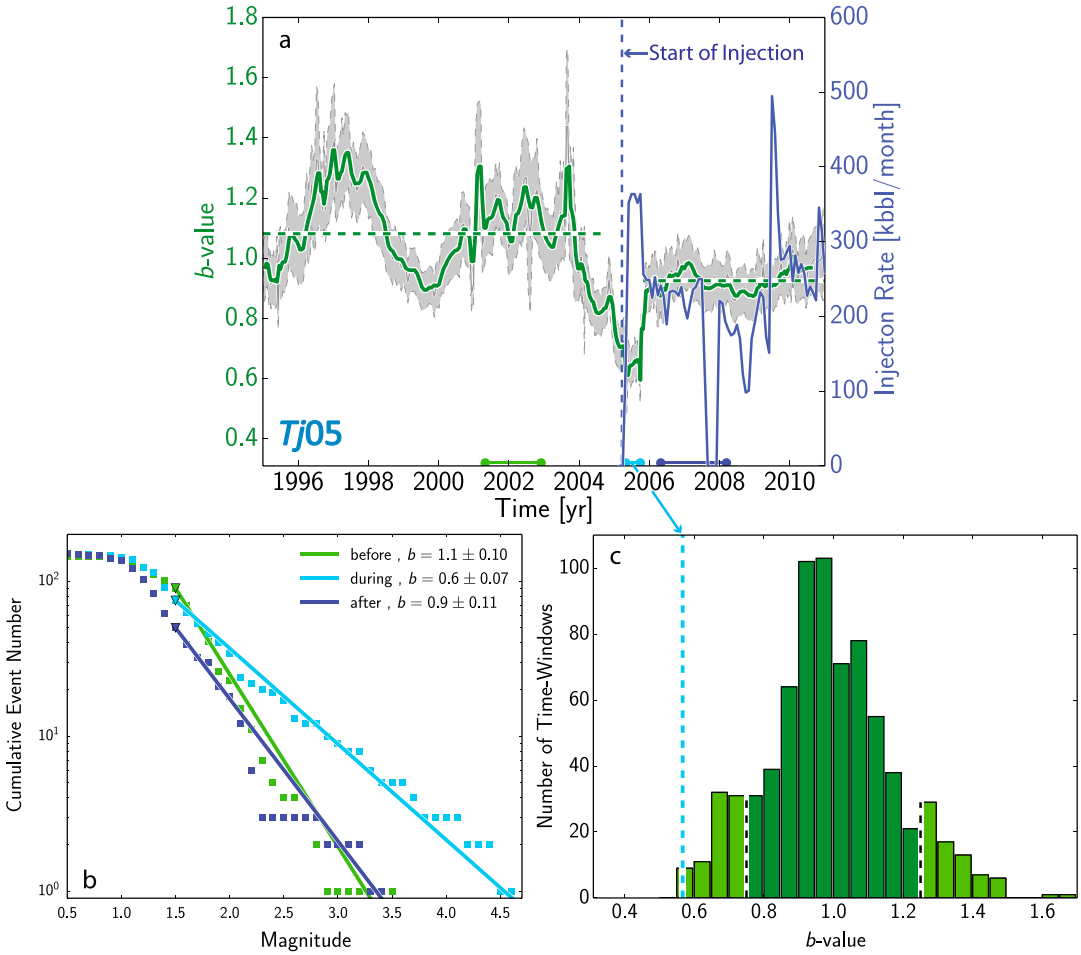

Figure 12. (a) Temporal *b* value variations (green) and corresponding standard deviations (gray) within a 15 km radius of injection site *Tj* between 1995 and 2011. Average *b* values before and after injection are highlighted by green, dashed lines. (b) Frequency-magnitude distributions and maximum-likelihood estimates of *b* values for three different periods, before, during, and after peak injection. The corresponding time windows are highlighted in Figure 12a with the same colors. (c) Distribution of temporal *b* value variation estimates between 1980 and 2011. The periods of low *b* value during injection fall outside of the confidence limits of the average *b* value of unity and can thus be considered as anomalous for the region.

automated search. This guided the definition of type *a* and type *b* injection episodes. The parameters of the search algorithm were then either fixed by statistical considerations or conservative estimates or their values were scanned over a wide range. We searched through the entire parameter space of injection rate thresholds for both type *a* and type *b* triggers. Moreover, some of the utilized tests such as the *R* statistic are nonparametric so no "tuning" was possible. Other parameters like maximum space-time windows for the short-term correlations are chosen as conservatively as possible given data constrains and need for statistically significant results.

Seismicity sequences may be induced at time scales that exceed the here selected time window but will likely be indistinguishable from the background seismicity according to equation (3). In other words, if induced seismicity sequences occur too far from the well or too long after a trigger onset, they will be indistinguishable from the background especially in tectonically active regions. Furthermore, a statistically significant correlation between injection and seismic activity is more challenging in wells with numerous triggers. This is partially a result of the resolution at which injection activity is recorded at present so that more precise trigger definitions are possible, for example, when daily injection rates become available.

Our study highlights the importance of an a priori definition of trigger criteria, to objectively estimate the seismogenic consequences of injection within an area. Other operational parameters can plausibly be used to search for induced seismicity, (e.g., total injection volumes or net production), although, based on our

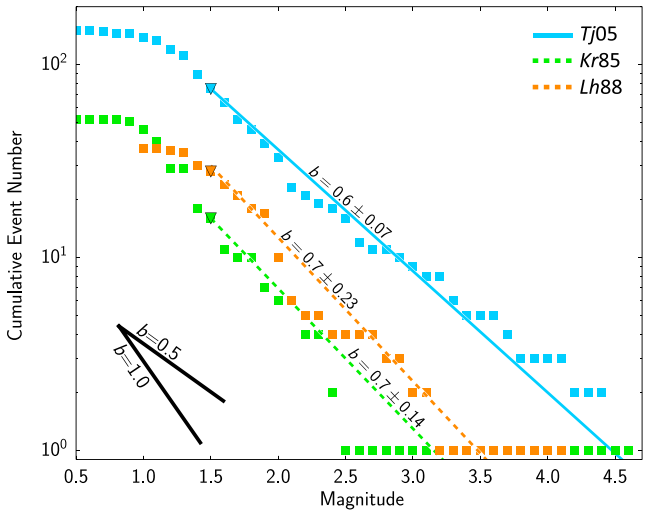

Figure 13. Comparison between frequency-magnitude distributions of seismicity sequences that approximately coincided with the onset of the triggers *Tj*05, *Kr*85, and *Lh*88. The corresponding time windows are 150, 360, and 230 days. The *b* values of all three sequences are comparably low.

exploratory data examination and applying the OISC method, we find that abrupt changes in injection rates have the largest seismogenic consequences in San Joaquin Valley.

6.2. How Frequent Are Induced Events in Central California?

Wastewater injection-induced seismic activity in central CA is rare compared to the central and eastern U.S., where reports of potentially induced seismicity have increased since 2011. Our results in CA highlight that detailed knowledge of background seismicity rates is necessary for the detection of significant induced rate changes and should also be consider when analyzing data with varying magnitude of completeness such as temporary array deployments or U.S. transportable array data.

Apart from this study, only few reports suggested a connection between fluid injection and seismicity in California outside of geothermal reservoirs, e.g., related to hydraulic fracturing [*Kanamori and Hauksson*, 1992] or water flooding [*Teng et al.*, 1973]. This raises questions about possibly lower seismogenic consequences of fluid injection in regions of active faulting compared to intraplate regions. A recent statistical analysis of injection operations and seismicity rates in OK and CA suggested that specific geologic setting and stress state on shallow faults are the main controls on induced seismicity potential [*Goebel*, 2015]. Each fluid injection and resulting pore pressure perturbation probes the proximity to failure of near-surface faults within a specific area around the injection site. A lack of large-scale injection-induced seismicity rate increase in CA could be connected to strongly different strain rates between intraplate and plate boundary regions [*Harrington and Brodsky*, 2006]. This difference may result in distinct stress states on intraplate faults, so that these faults are more susceptible to remote triggering and injection-induced pressure changes than plate boundary regions [*van der Elst et al.*, 2013; *Keranen et al.*, 2014; *Goebel*, 2015]. Extending our identification scheme to more areas may help understand these differences in crustal stresses.

6.3. Induced Seismicity Classifications and Application of the OISC Method

The OISC method allows for a relative comparison between candidate-induced earthquake sequences based on the corresponding statistical measures. These measures provide the first step toward a relative ranking of cases of likely induced seismicity between more likely induced versus more likely tectonic. A relative ranking based on correlation statistics will be of increasing interest with the larger number of reported, induced seismicity cases within the central U.S. and elsewhere and will help encompass the inherent complexities in triggering processes. Such a ranking is included in Table 2 from least to most likely induced.

The OISC method differs in several important points from the previous work: (1) We define trigger criteria, i.e., a type and magnitude of injection activity, a priori, and apply them to the entire data set, i.e., the ~1400 wastewater disposal wells in Kern County. (2) Our initial observations, in agreement with many previous studies [e.g., *Hsieh and Bredehoeft*, 1981; *Kim*, 2013; *Keranen et al.*, 2014], suggest that the range of time windows, focal depths, and injection-affected areas can vary strongly in different areas. As a consequence, the

OISC method concentrates more strongly on the quality of correlations between injection and seismicity rate changes rather than limiting the analysis to small, near-injection space-time-depth windows. (3) We designed our method to be generally applicable based on the most widely available data sets. Consequently, we did not include detailed modeling of expected pore pressure perturbations on near-injection faults as, for example, suggested by *Davis and Frohlich* [1993]. This type of modeling requires more detailed knowledge about the subsurface beneath each injection site. Lastly, we tested if candidate events were simply aftershocks within an ongoing sequence, accounting for the more complex spatial-temporal clustering in seismically active regions.

In light of the difficulty to discriminate induced and tectonic earthquakes, some limitations of the OISC method should be considered as well. The OISC method evaluates correlations between episodes of injection rate changes and local seismicity rate changes, using the most widely available data sets. The corresponding statistical measures provide no physical test for whether a particular earthquake sequence is purely human induced. We have shown that the complex spatial-temporal clustering of likely induced sequences in tectonically active regions prevents a simple binary decision of tectonic versus induced earthquakes. Instead, a more meaningful categorization should include the relative contributions from both types of forces, similar to studies of natural earthquake swarms [*Hainzl and Ogata*, 2005]. We limited the current study to the two most plausible types of injection activity as possible earthquake triggers which were based on an exploratory inspection of injection activity and nearby seismicity sequences. If data availability and resolution is adequate, these types of triggers can be extended. Furthermore, the present study predominantly focused on quantifying the strength of correlations between short-term injection and seismicity rate changes. More restrictive distance cutoffs may be feasible in regions where local geology, hypocenter locations, and focal depths are known to greater accuracy. The latter are poorly constrained in our study area and were thus not included in the general identification method. More details about the focal depth estimates can be found in section S5 in the supporting information.

6.4. Triggering Mechanisms and Expected Maximum Magnitude

Fluid injection-induced earthquake sequences are commonly attributed to a decrease in effective stress caused by pore pressure increase on a fault surfaces [e.g., *Evans*, 1966; *Healy et al.*, 1968; *Raleigh et al.*, 1976; *McGarr*, 2014]. The pore pressure perturbation is driven by a diffusive process and results in characteristic migration patterns over small space-time windows as observed for *Kr*85.

To understand the seismic hazard presented by fluid injection, it is vital to estimate the expected maximum magnitude of induced earthquake sequences. Recently, *McGarr* [2014] suggested a linear relationship between the total change in injected volume, ΔV, and the expected maximum moment release, M_0^{max}, of the largest-magnitude induced event, using the volume of injected fluid as a proxy for pressure changes in the subsurface. In Figure 14, we show McGarr's relationship within the context of the here identified and previously reported cases of likely induced earthquake sequences. The locations of reported induced seismicity in Figure 14 are KTB = eastern Bavaria, Germany; BUK = Bowland shale, United Kingdom; GAR = Garvin County, OK; STZ = Soultz, France; DFW = Dallas-Fort Worth Airport, TX; BAS = Basel, Switzerland; ASH = Ashtabula, OH; CBN = Cooper Basin, Australia; ASH = Ashtabula, OH; YOH = Youngstown, OH; PBN = Paradox Valley, CO; RAT1 = Raton Basin, CO; GAK = Guy, AR; POH = Painesville, OH; RMA = Denver, CO; TTX = Timpson, TX; RAT2 = Raton Basin, CO; and POK = Prague, OK. The reported sequences include induction by hydraulic fracturing, wastewater disposal, and geothermal reservoir stimulation [see *McGarr*, 2014, and references therein]. In our study, the largest event connected to *Tj*05 exceeds the upper limit, M_0^{max}, indicating that induced earthquake ruptures may extend beyond the injection-affected volume. However, the Tejon region experienced wastewater disposal in additional wells so that the cumulative injection volume that contributed to the creation of the largest-magnitude event may be higher.

The synthesis of previous and here identified likely induced sequences highlights a general correlation between the maximum injected volume and resulting moment release (Figure 14). This correlation may originate from an underlying physical connection as suggested by *McGarr* [2014] but may also stem from a stochastic process related to the fractal geometry of fault networks. Smaller faults are generally more abundant and more readily triggered. Nevertheless, larger faults may be activated as a result of increasing injection volumes and injection-affected areas resulting in the observed correlation between injected volume and moment release.

While some foreshocks were detected prior to larger magnitude events in sequence *Kr*85, seismic events within a ~5 km area of the injection sites are rare (see Figure 6). This may be caused by a lack of critically

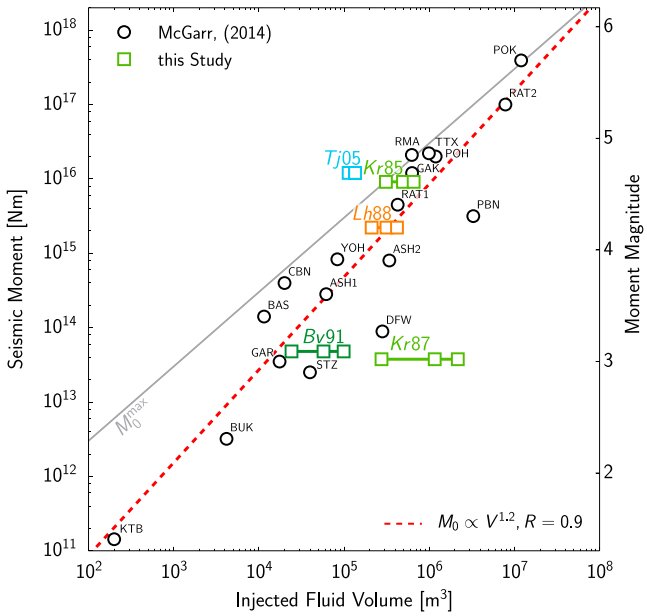

Figure 14. Total injected volume and seismic moment (for simplicity, we assume $M_L = M_w$) of the largest-magnitude, likely induced earthquakes compiled by *McGarr* [2014] (black circles) and for sequences *Tj*05, *Lh*88, *Kr*85, and *Kr*87 (squares). For completeness, we also included a M_L 3.1 event that occurred during peak injection close to *Bv* and is labeled *Bv*91. We estimated injection volumes by summing injection rates over 2, 5, and 11 months prior to trigger onsets (three different frames from left to right). The red line shows the least squares fit of the log-transformed data and the gray line is the maximum predicted seismic moment release from *McGarr* [2014].

stressed faults close to the injection wells, especially for injection sites in sedimentary basins. Shallow sedimentary layers store less tectonic strain energy and exhibit predominantly velocity-strengthening frictional behavior at upper crustal conditions, resulting in low stress drops and little to no detectable seismic activity in close proximity to the injection sites [*Das and Scholz*, 1983; *Scholz*, 1998]. On the other hand, advancing pore pressure fronts may affect increasing areas and the probability of encountering a critically stressed fault within basement layers or toward the edge of a basin increases, which may explain the observations related to the likely induced sequences *Kr*85 and *Tj*05. The subsequently activated faults may not always be the closest mapped faults depending on crustal structure, fault strengths and stress distributions. Preexisting faults and high-permeability reservoir structures may also act as fluid conduits and may lead to localized pore pressure increase that extends to several kilometers from the injection sites [*Hsieh and Bredehoeft*, 1981; *Zhang et al.*, 2013; *Keranen et al.*, 2014].

Our results suggest a relatively higher triggering potential of abrupt changes in injection rates. Rapid injection rate changes prior to seismic activity have also been observed in previous studies, e.g., in Rocky Mountain arsenal, CO, in 1965 [e.g., *Hsieh and Bredehoeft*, 1981] and more recently, in 2011, during wastewater injection close to Youngstown, OH [*Kim*, 2013], and may indicate a contribution from poroelastic stresses during earthquake triggering. Poroelastic stresses are a function of the fluid density and elastic properties of the rock matrix but also of the net change in fluid mass per unit volume [*Segall*, 1989]. The net change of fluid mass is highest close to the pore pressure front which may explain the relatively localized occurrence of seismicity close to the arrival of the initial pressure pulse observed for some of the here identified sequences.

6.5. *b* Value Variations of Induced Seismicity

We identified three likely induced earthquake sequences that showed anomalously low *b* values. Low *b* values during injection activity have been reported previously for injection-induced seismicity in Ohio [*Skoumal et al.*, 2014], China [*Lei et al.*, 2008], and the Geysers region, northern California [*Martínez-Garzón et al.*, 2014]. Other studies suggest *b* values to be higher for injection-induced seismicity close to injection and within the central U.S. [e.g., *Bachmann et al.*, 2011; *Petersen et al.*, 2015].

Generally, variations in *b* value should be interpreted carefully because of the inherent uncertainties in estimating power law exponents over a limited number of decades and from seismicity records with changing quality over time. Moreover, a precise correlation between *b* value variations and other time series,

e.g., injection rates, is complicated by different temporal resolutions. Thus, the most robust features within our data are generally low *b* values during the time of peak injection rates.

Changes in *b* values and frequency-magnitude distributions may originate from different underlying physical processes [e.g., *Richardson and Jordan*, 2002] and can also be caused by a gradual activation of fault structures [e.g., *Downie et al.*, 2010; *Goebel et al.*, 2013]. Low *b* values may mark a transition of seismic activity from a 3-D fractal fracture network to a 2-D fault zone associated with the gradual activation of faults by increasing pore pressures [*King*, 1983]. These gradual activation processes may in addition concentrate stresses at load-bearing asperities which increase the probability of ruptures to grow to larger sizes thereby decreasing *b* values below commonly observed values of unity [e.g., *Wiemer and Wyss*, 1997; *Goebel et al.*, 2012, 2013].

7. Conclusions

We have developed a method to identify likely induced seismicity sequences objectively, based on correlating short-term injection and seismicity rate changes and applied our method to Kern County, California, thereby assessing if $M > 3$ earthquake sequences may have been induced by wastewater disposal. We identified four likely induced seismicity sequences that were associated with abrupt changes in wastewater injection rates of 200 kbbl/month or more. These sequences showed events with magnitudes up to M_w4.7. We observed seismicity migration characteristics that are expected for triggering by pore pressure diffusion. However, we also observed one case of injection activity for which seismicity migrated linearly in space and time, indicating processes beyond simple, isotropic pressure diffusion. The identified, likely induced seismicity sequences generally show low Gutenberg-Richter *b* values between 0.6 and 0.7, possibly related to a more gradual fault activation process. The relative scarcity of induced seismicity detected by the OISC method and lack of large-scale seismicity rate increase in Kern County indicates that the seismogenic consequences of fluid injection are generally low in the area. Through an application of our method in other regions, the seismogenic consequences of fluid injection can be assessed at larger scales in the future. Such an assessment can advance the understanding of dominating triggering processes and can provide an important step toward a quantitative definition of injection-induced earthquakes and the expected seismic hazard.

Acknowledgments

We thank Frederic Cappa, Jason Saleeby, Emily Brodsky, Tayeb Tafti and the members of the Induced Seismicity Consortium at USC for helpful discussions. We thank the statistical seismology community for the Community Online Resources for Statistical Seismicity Analysis (corssa.org) and Jeremy Zechar for providing his declustering code. This research was supported by NEHRP/USGS grants G13AP00047 and G14AP00075, and by the Southern California Earthquake Center (SCEC) under contribution number 12017. SCEC is funded by NSF Cooperative Agreement EAR-0529922 and USGS Cooperative Agreement 07HQAG0008. The utilized seismicity catalog and injection data of likely earthquake-inducing wells is available in the supporting information. The computer program for running the OISC algorithm was developed using the open-source python programming language and is available from the first author upon request.

References

Akaike, H. (1974), A new look at the statistical model identification, *IEEE Trans. Autom. Control*, *19*(6), 716–723.

Bachmann, C. E., S. Wiemer, J. Woessner, and S. Hainzl (2011), Statistical analysis of the induced Basel 2006 earthquake sequence: Introducing a probability-based monitoring approach for enhanced geothermal systems, *Geophys. J. Int.*, *186*, 793–807, doi:10.1111/j.1365-246X.2011.05068.x.

Bachmann, C. E., S. Wiemer, B. P. Goertz-Allmann, and J. Woessner (2012), Influence of pore-pressure on the event-size distribution of induced earthquakes, *Geophys. Res. Lett.*, *39*, L09302, doi:10.1029/2012GL051480.

Brodsky, E. E., and L. J. Lajoie (2013), Anthropogenic seismicity rates and operational parameters at the Salton Sea Geothermal Field, *Science*, *341*(6145), 543–546.

CA Department of Conservation (2012), Division of oil, gas and geothermal resources: Production history in California. [Available at ftp://ftp.consrv.ca.gov/pub/oil/annual_reports, accessed Sept. 26, 2014.]

Clauset, A., C. R. Shalizi, and M. E. J. Newmann (2009), Power-law distributions in empirical data, *SIAM Rev.*, *51*(4), 661–703.

Das, S., and C. Scholz (1983), Why large earthquakes do not nucleate at shallow depths, *Nature*, *305*, 621–623.

Davis, S. D., and C. Frohlich (1993), Did (or will) fluid injection cause earthquakes?—Criteria for a rational assessment, *Seismol. Res. Lett.*, *64*(3–4), 207–224.

Deichmann, N., and D. Giardini (2009), Earthquakes induced by the stimulation of an enhanced geothermal system below Basel (Switzerland), *Seismol. Res. Lett.*, *80*(5), 784–798.

Downie, R., E. Kronenberger, and S. Maxwell (2010), Using microseismic source parameters to evaluate the influence of faults on fracture treatments: A geophysical approach to interpretation, SPE 134772 presented at SPE Annual Technical Conference and Exhibition, 19–22 Sept., Florence, Italy, doi:10.2118/134772-MS.

Ellsworth, W. L. (2013), Injection-induced earthquakes, *Science*, *341*(6142), 1–7, doi:10.1126/science.1225942.

Evans, D. (1966), The Denver area earthquakes and the rocky mountain arsenal disposal well, *Mt. Geol.*, *1*(1), 23–36.

Felzer, K. R., and E. E. Brodsky (2005), Testing the stress shadow hypothesis, *J. Geophys. Res.*, *110*, B05S09, doi:10.1029/2004JB003277.

Felzer, K. R., T. W. Becker, R. E. Abercrombie, G. Ekström, and J. R. Rice (2002), Triggering of the 1999 M_w 7.1 Hector Mine earthquake by aftershocks of the 1992 M_w 7.3 Landers earthquake, *J. Geophys. Res.*, *107*(B9), 2190, doi:10.1029/2001JB000911.

Frohlich, C. (2012), Two-year survey comparing earthquake activity and injection-well locations in the Barnett Shale, Texas, *Proc. Natl. Acad. Sci.*, *109*(35), 13,934–13,938.

Frohlich, C., and M. Brunt (2013), Two-year survey of earthquakes and injection/production wells in the Eagle Ford Shale, Texas, prior to the M_w 4.8 20 October 2011 earthquake, *Earth Planet. Sci. Lett.*, *379*, 56–63.

Gardner, J. K., and L. Knopoff (1974), Is the sequence of earthquakes in Southern California, with aftershocks removed, Poissonian?, *Bull. Seismol. Soc. Am.*, *64*(5), 1363–1367.

Goebel, T. H. W. (2015), A comparison of seismicity rates and fluid injection operations in Oklahoma and California: Implications for crustal stresses, *Leading Edge*, *34*(6), 640–648, doi:10.1190/tle34060640.1.

Goebel, T. H. W., T. W. Becker, D. Schorlemmer, S. Stanchits, C. Sammis, E. Rybacki, and G. Dresen (2012), Identifying fault hetergeneity through mapping spatial anomalies in acoustic emission statistics, *J. Geophys. Res.*, *117*, B03310, doi:10.1029/2011JB008763.

Goebel, T. H. W., D. Schorlemmer, T. W. Becker, G. Dresen, and C. G. Sammis (2013), Acoustic emissions document stress changes over many seismic cycles in stick-slip experiments, *Geophys. Res. Letts.*, *40*, 2049–2054, doi:10.1002/grl.50507.
Goebel, T. H. W., T. W. Becker, C. G. Sammis, and G. Dresen (2014a), Off-fault damage and acoustic emission distributions during the evolution of structurally-complex faults over series of stick-slip events, *Geophys. J. Int.*, *197*, 1705–1718, doi:10.1093/gji/ggu074.
Goebel, T. H. W., T. Candela, C. G. Sammis, T. W. Becker, G. Dresen, and D. Schorlemmer (2014b), Seismic event distributions and off-fault damage during frictional sliding of saw-cut surfaces with predefined roughness, *Geophys. J. Int.*, *196*(1), 612–625, doi:10.1093/gji/ggt401.
Hainzl, S., and Y. Ogata (2005), Detecting fluid signals in seismicity data through statistical earthquake modeling, *J. Geophys. Res.*, *110*, B05S07, doi:10.1029/2004JB003247.
Hardebeck, J. L. (2006), Homogeneity of small-scale earthquake faulting, stress, and fault strength, *Bull. Seismol. Soc. Am.*, *96*(5), 1675–1688.
Harrington, R. M., and E. E. Brodsky (2006), The absence of remotely triggered seismicity in Japan, *Bull. Seismol. Soc. Am.*, *96*, 871–878.
Hauksson, E., W. Yang, and P. M. Shearer (2012), Waveform relocated earthquake catalog for Southern California (1981 to June 2011), *Bull. Seism. Soc. Am.*, *102*(5), 2239–2244.
Healy, J., W. Rubey, D. Griggs, and C. Raleigh (1968), The Denver earthquakes, *Science*, *161*(3848), 1301–1310.
Horton, S. (2012), Disposal of hydrofracking waste fluid by injection into subsurface aquifers triggers earthquake swarm in central Arkansas with potential for damaging earthquake, *Seismol. Res. Lett.*, *83*(2), 250–260.
Hsieh, P. A., and J. D. Bredehoeft (1981), A reservoir analysis of the Denver earthquakes: A case of induced seismicity, *J. Geophys. Res.*, *86*(B2), 903–920.
Kanamori, H., and E. Hauksson (1992), A slow earthquake in the Santa Maria basin, California, *Bull. Seismol. Soc. Am.*, *82*(5), 2087–2096.
Keranen, K., M. Weingarten, G. Abers, B. Bekins, and S. Ge (2014), Sharp increase in central Oklahoma seismicity since 2008 induced by massive wastewater injection, *Science*, *345*(6195), 448–451.
Keranen, K. M., H. M. Savage, G. A. Abers, and E. S. Cochran (2013), Potentially induced earthquakes in Oklahoma, USA: Links between wastewater injection and the 2011 M_w 5.7 earthquake sequence, *Geology*, *41*(6), 699–702.
Kim, W.-Y. (2013), Induced seismicity associated with fluid injection into a deep well in Youngstown, Ohio, *J. Geophys. Res. Solid Earth*, *118*, 3506–3518, doi:10.1002/jgrb.50247.
King, G. C. P. (1983), The accommodation of large strains in the upper lithosphere of the earth and other solids by self-similar fault systems: The geometrical origin of *b*-value, *Pure Appl. Geophys.*, *121*, 761–814.
Lei, X., G. Yu, S. Ma, X. Wen, and Q. Wang (2008), Earthquakes induced by water injection at ~3 km depth within the Rongchang gas field, Chongqing, China, *J. Geophys. Res.*, *113*, B10310, doi:10.1029/2008JB005604.
Martínez-Garzón, P., M. Bohnhoff, G. Kwiatek, and G. Dresen (2013), Stress tensor changes related to fluid injection at The Geysers geothermal field, California, *Geophys. Res. Lett.*, *40*, 2596–2601, doi:10.1002/grl.50438.
Martínez-Garzón, P., G. Kwiatek, H. Sone, M. Bohnhoff, G. Dresen, and C. Hartline (2014), Spatiotemporal changes, faulting regimes, and source parameters of induced seismicity: A case study from The Geysers geothermal field, *J. Geophys. Res. Solid Earth*, *119*, 8378–8396, doi:10.1002/2014JB011385.
McGarr, A. (2014), Maximum magnitude earthquakes induced by fluid injection, *J. Geophys. Res. Solid Earth*, *119*, 1008–1019, doi:10.1002/2013JB010597.
Petersen, M. D., et al. (2015), Incorporating induced seismicity in the 2014 United States National Seismic Hazard Model: Results of the 2014 workshop and sensitivity studies, *U.S. Geol. Surv. Open File Rep. 2015-1070*, U.S. Geol. Surv. Resto, Va.
Raleigh, C., J. Healy, and J. Bredehoeft (1976), An experiment in earthquake control at Rangely, Colorado, *Science*, *191*(4233), 1230–1237.
Richardson, E., and T. H. Jordan (2002), Seismicity in deep gold mines of south Africa: Implications for tectonic earthquakes, *Bull. Seismol. Soc. Am.*, *92*, 1766–1782, doi:10.1785/0120000226.
Rubinstein, J. L., W. L. Ellsworth, A. McGarr, and H. M. Benz (2014), The 2001-present induced earthquake sequence in the Raton Basin of northern New Mexico and southern Colorado, *Bull. Seismol. Soc. Am.*, *104*, 2162–2181.
Schoenball, M., L. Dorbath, E. Gaucher, J. F. Wellmann, and T. Kohl (2014), Change of stress regime during geothermal reservoir stimulation, *Geophys. Res. Lett.*, *41*, 1163–1170, doi:10.1002/2013GL058514.
Scholz, C. (1998), Earthquakes and friction laws, *Nature*, *391*(6662), 37–42.
Segall, P. (1989), Earthquakes triggered by fluid extraction, *Geology*, *17*(10), 942–946.
Segall, P., J.-R. Grasso, and A. Mossop (1994), Poroelastic stressing and induced seismicity near the Lacq gas field, southwestern France, *J. Geophys. Res.*, *99*(B8), 15,423–15,438.
Shapiro, S. A., E. Huenges, and G. Borm (1997), Estimating the crust permeability from fluid-injection-induced seismic emission at the KTB site, *Geophys. J. Int.*, *131*, F15–F18.
Skoumal, R. J., M. R. Brudzinski, B. S. Currie, and J. Levy (2014), Optimizing multi-station earthquake template matching through re-examination of the Youngstown, Ohio, sequence, *Earth Plant. Sc. Lett.*, *405*, 274–280, doi:10.1016/j.epsl.2014.08.033.
Sumy, D. F., E. S. Cochran, K. M. Keranen, M. Wei, and G. A. Abers (2014), Observations of static Coulomb stress triggering of the November 2011 M5.7 Oklahoma earthquake sequence, *J. Geophys. Res. Solid Earth*, *119*, 1904–1923, doi:10.1002/2013JB010612.
Teng, T. L., C. R. Real, and T. L. Henyey (1973), Microearthquakes and water flooding in Los Angeles, *Bull. Seismol. Soc. Am.*, *63*(3), 859–875.
Unruh, J., E. Hauksson, and C. H. Jones (2014), Internal deformation of the southern Sierra Nevada microplate associated with foundering lower lithosphere, California, *Geophere*, *10*, 107–128, doi:10.1130/GES00936.1.
Utsu, T. (1999), Representation and analysis of the earthquake size distribution: A historical review and some approaches, *Pure Appl. Geophys.*, *155*, 509–535.
van der Elst, N. J., and E. E. Brodsky (2010), Connecting near-field and far-field earthquake triggering to dynamic strain, *J. Geophys. Res.*, *115*, B07311, doi:10.1029/2009JB006681.
van der Elst, N. J., H. M. Savage, K. M. Keranen, and G. A. Abers (2013), Enhanced remote earthquake triggering at fluid-injection sites in the midwestern United States, *Science*, *341*(6142), 164–167.
van Stiphout, T., J. Zhuang, and D. Marsan (2012), Seismicity declustering, *Community Online Resource for Statistical Seismicity Analysis*, ETH - Swiss Federal Inst. of Technol. Zurich, doi:10.5078/corssa-52382934. [Available at http://www.corssa.org.]
Wiemer, S., and M. Wyss (1997), Mapping the frequency-magnitude distribution in asperities: An improved technique to calculate recurrence times?, *J. Geophys. Res.*, *102*, 15,115–15,128.
Yang, W., and E. Hauksson (2013), The tectonic crustal stress field and style of faulting along the Pacific North America Plate boundary in Southern California, *Geophys. J. Int.*, *194*(1), 100–117.
Zhang, Y., et al. (2013), Hydrogeologic controls on induced seismicity in crystalline basement rocks due to fluid injection into basal reservoirs, *Ground Water*, *51*(4), 525–538.